Eur. Phys. J. Special Topics **227**, 167–177 (2018)
© EDP Sciences, Springer-Verlag GmbH Germany, part of Springer Nature, 2018
https://doi.org/10.1140/epjst/e2018-00057-1

THE EUROPEAN PHYSICAL JOURNAL SPECIAL TOPICS

Regular Article

# On the tensile resistance of UHPC at impact

Kerstin Weinberg and Mohammad Reza Khosravani[a]

Chair of Solid Mechanics, Department of Mechanical Engineering, University of Siegen, Paul-Bonatz-Str. 9-11, 57068 Siegen, Germany

Received 28 July 2017 / Received in final form 18 December 2017
Published online 10 September 2018

**Abstract.** Ultra-High Performance Concrete (UHPC) is a new class of concrete which shows high strength and durability. In this paper experimental investigations on the dynamic properties of a low-silica UHPC are presented. By means of Hopkinson Pressure Bar experiments the dynamic elastic modulus and the tensile resistance of the material are determined. Additional numerical fracture simulations, based on a cohesive finite element technique, confirm the measured data and illustrate the possibilities to obtain predictive simulations.

## 1 Introduction

Ultra-High Performance Concrete (UHPC) is a new generation of concrete with superior strength which allows to build filigran architectures and protective safety structures [1]. The development of UHPC is an ongoing and gradual process which needs to go hand in hand with mechanical testing procedures. Classical experiments determine the concrete's elasticity as well as its compressive and flexural strength under static loading conditions. Dynamic properties, however, such as impact strength, dynamic tensile resistance and failure criteria are hard to obtain under reproducible conditions.

Split-Hopkinson Pressure Bar (SHPB) experiments are common arrangements to measure the material properties in impact loading [2–7]. In a conventional SHPB setup the specimen is placed between the ends of two straight bars and a stress pulse is created which propagates through bars and specimen, see Figure 1. Stresses and strains are measured to deduce the specimen's elastic properties at high strain rates. For spalling experiments the Hopkinson-Pressure Bar (HPB) setup is modified in such a way, that the bar is not 'split' anymore, i.e., the transmission bar is omitted and instead a longer specimen is placed at the end of the incident bar. This test arrangement allows to obtain the failure strength of brittle materials such as concrete, cf. [8–16].

UHPC is by definition a high strength material. Depending on the ingredients, the special mixture and the curing process, the compressive strength of pure UHPC exceeds values of 150 MPa. Like common concrete it has also a significant tension-compression anisotropy, i.e., the tensile resistance of UHPC is less than one-tenth of its compressive strength. We exploit this anisotropy to perform spallation experiments in order to determine the UHPC's tensile resistance. Unlike classical concrete UHPC

[a] e-mail: mohammadreza.khosravani@uni-siegen.de

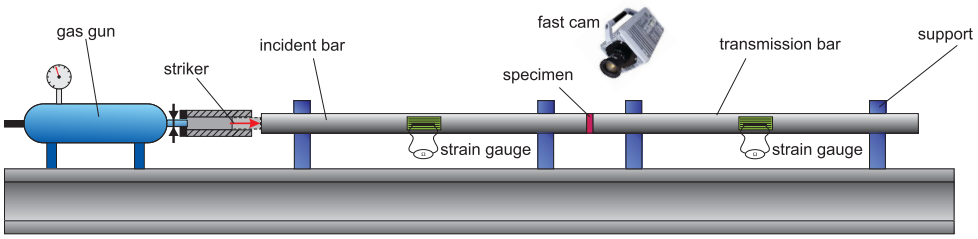


**Fig. 1.** Setup for Split-Hopkinson Pressure Bar (SHPB) experiments.

has a very fine and homogenous structure with a hardly visible size of aggregates. This allows us to use small specimens, similar to the ones used for ceramics in [17,18].

In the following we present a strategy to determine the failure strength of a specific low-silica UHPC mixture (without additional reinforcing fibres). The paper is structured as follows: Some information about the preparation of the UHPC specimen and the measuring equipment are provided in Section 2. In Sections 3 and 4 we present our experiments to determine the elastic modulus and the tensile resistance, respectively, and we evaluate the accuracy of the chosen method. A numerical fracture computation based on a finite element analysis (FEA) is outlined in Section 5 together with parametric studies on the plausibility of our experimental results. A short summary in Section 6 concludes the paper.

## 2 Specimen preparation and technical details

Like common concrete UHPC is a composition of cement, water, admixtures, additives and aggregates of different sizes. Its mechanical properties are improved by a lower water to cement ratio, a higher packing density and specific additives. This results in a fine and almost homogeneous microstructure with very low porosity. Responsible for the superior properties of UHPC is a large amount of sub-micrometer silica. This silica, however, makes the mixture corrosive and is restricted for common concrete. For example, German standards limit the amount of silica to 11%, cf. [19], and therefore, in this research a UHPC mixture with an amount of only 10% microsilica is tested. Details of the composition are summarized in Table 1; the static properties determined in accordance to DIN EN 12390-3 and DIN EN 12390-5 are also presented there.

The cylindrical specimen of 20 mm diameter were produced by filling the concrete into specially designed, hollow copper tubes with a length of 250 mm. The tubes allow for an easy extraction of the samples after the first 24 h of hardening. For filling the UHPC was horizontally injected into the tube by a special syringe and a concrete overflow was produced at the end of the tubes to cast off air bubbles in the concrete induced by the injection process. The tubes were then mounted vertically, closing the bottom, and each tube was fully filled with UHPC. Because densifying the concrete with a common plate compactor was not possible, a wire was used for manual densification and degassing after the filling process. The specimens were then stored under water at 20 °C for at least 28 days of hardening. Because the outer parts of the produced raw-samples could be impaired by sedimentation and air injection due to the filling and the vertical storage, all specimens were taken from the middle of the raw-samples. The samples were precisely cut into their required lengths of 200 mm by a linear precision saw with a diamond cutting disc. This ensured that all

**Table 1.** Composition of the UHPC mixture in mass proportion normalized by cement and static strength according to DIN EN 12390 standard.

| | | | |
|---|---|---|---|
| Cement | 1.00 | | |
| Quartz sand | 0.94 | Compressive strength [MPa] | $186 \pm 3.1$ |
| Quartz powder | 0.34 | Flexural strength [MPa] | $14.4 \pm 0.3$ |
| Microsilica | 0.10 | Raw density [kg/m$^3$] | 2374.81 |
| Water | 0.23 | Grain size [$\mu$m] | 725 |
| Superplasticizer | 0.03 | | |

specimens have flat surfaces and, in particular, that the free ends are perpendicular to the symmetry axis.

Additionally, short specimens of 20 mm length were cut out of the samples. A comparison between the densities of the fresh concrete, calculated by use of a concrete volume calculation, and the measured densities of the hardened concrete served as an examination for quality of the concrete, cf. [20].

In the HPBs the strain is measured by means of strain gauges with a resistance of $120.0 \pm 0.1\ \Omega$ and a gauge factor of 2.07. All data obtained from the gauges are acquired by a HBM GEN7t system with a maximum sampling rate of 100 mega samples per second. Using a dual rate recording principle, long term observations can be recorded while rapidly occurring events can be captured concurrently. Moreover, a high speed video camera (FASTCAM SA5) with capability of clear recording in low-light and with a maximum rate of 775,000 frames per second (fps) is used as non-contact optical technique to record the spallation process. The light sensitive sensor of the camera provides a 12-bit analogue to digital converter with 17 $\mu$m pixel size without interpolation. In order to record the velocities in the spalling experiment, 39 points are marked on each specimen and tracked with a recording rate of 262,500 fps. Out of this information a specifically developed MATLAB based image correlation software calculates the velocity data.

## 3 Determination of the dynamic elastic modulus

For the conventional SHPB setup two aluminum bars of 1800 mm length are used as incident and transmission bar. A short UHPC specimen is placed between them. Bars and specimen have a diameter of 20 mm. The impact of an accelerated, 100 mm long steel striker with a mass of 250 g generates a compressive pressure pulse which propagates through the bars. The pulse is measured as strain signal in the middle of the incident and the transmission bar and the strain in the specimen $\epsilon_s$ is calculated from a superposition of these signals.

$$\epsilon_s(t) = \frac{u_2(t) - u_1(t)}{l_s} = \frac{c_b}{l_s} \int_o^t (\epsilon_I(\bar{t}) - \epsilon_R(\bar{t}) - \epsilon_T(\bar{t}))\ \mathrm{d}\bar{t}. \tag{1}$$

Here $u_1$ and $u_2$ denote the axial displacements at the specimen-incident-bar interface and the specimen-transmission-bar interface, i.e, the begin and the end of the specimen, $l_s = 20$ mm is its length. The longitudinal wave speed $c_b$ depends on elastic modulus and mass density, $c_b = \sqrt{E_b/\rho_b}$. Here and below the indices $I, R$ and $T$ refer to incident, reflected and transmitted wave, respectively. The compressive loading is properly calibrated to obtain a constant strain-rate. Specifically, we used layers of t paper and aluminum paper with a total thickness of 0.8 mm and a diameter of 10 mm. The measured strain signal is displayed in Figure 2. The linear slope of the strain pulse indicates a constant strain rate after $\approx 50\,\mu$s.

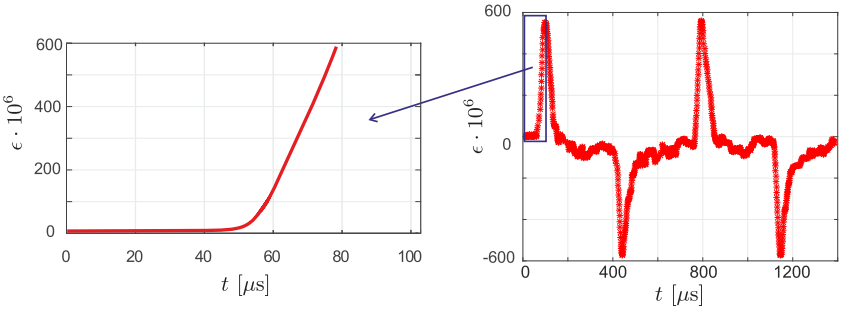


**Fig. 2.** Strain pulse measures at the incident bar for a striker velocity of 6.5 m/s.

Assuming instantaneous equilibrium in the specimen the SHPB relations for stress and strain are derived, cf. [21,22],

$$\sigma_s = \frac{E_b A_b}{2A_s}\left(\epsilon_I - \epsilon_R - \epsilon_T\right) = E_b \frac{A_b}{A_s}\epsilon_T, \tag{2}$$

$$\dot{\epsilon}_s = \frac{v_1 - v_2}{l_s} = -2\frac{c_b}{l_s}\epsilon_R, \tag{3}$$

where $E_b$ is the elastic modulus of the bars; $A_b$ and $A_s$ are the cross-sectional areas of bar and specimen. Combining the equations 2 and 3 gives the dynamic elastic modulus of the specimen,

$$E_{\mathrm{dyn}} = \frac{\sigma_s}{\epsilon_s} = -\frac{A_b E_b \epsilon_T l_s}{2A_s c_b \int_0^t \epsilon_R \,\mathrm{d}t}\,. \tag{4}$$

Typically, the dynamic elastic modulus is higher than the corresponding static value, an effect which is at least partially attributed to lateral inertia of the specimen in a SHPB setup, see [23–25] for a discussion. Furthermore, the SHPB equations base on simplifying assumptions such as: the one-dimensional wave theory describes the pulse propagation in the bars; there is instantaneous stress equilibrium in the loaded specimen; all inertia and friction effects are negligible. The equilibrium condition basically states, that the reaction force on the specimen-transmission bar interface is the same as the incoming force on the specimen-incident bar interface. This assumption corresponds to an axially uniform state of deformation which requires a short and homogenous specimen.

Repeated tests on 15 different UHPC specimens were performed with a striker velocity of 6.5 m/s. Calculated with equation 2 the signal gives a strain rate of $\dot{\epsilon} = 28.5\,\mathrm{s}^{-1}$. For our UHPC mixture the obtained dynamic elastic modulus is:

$$E_{\mathrm{dyn}} = 51.3 \pm 0.5\,\mathrm{GPa},$$

where the result is given with standard deviation. This value is similar to the static elastic modulus of 43–50 GPa reported, e.g., in [26,27]. Regarding the moderate strain rate and the small size of our specimen the measured $E_{\mathrm{dyn}}$ is in the expected range.

Alternatively to the above calculation, the dynamic elastic modulus can also be determined from the wave speed $c_s$, cf. [21],

$$E_{\mathrm{dyn}} = \rho_s c_s^2, \tag{5}$$

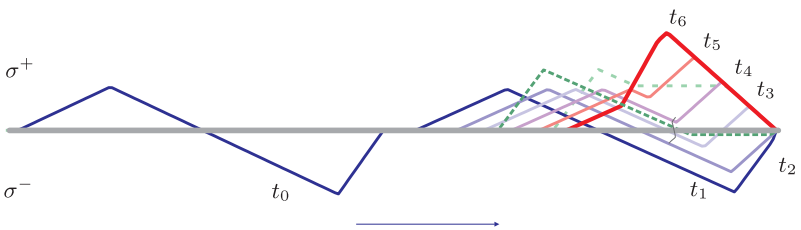


**Fig. 3.** Illustration of the superposition of incident and reflected stress wave in a spallation experiment—$t_0$: incoming pressure wave pulse, $t_1$: begin of reflection at the free end, $t_2 - t_5$: superposition during reflection with peak stress $t_6$. Between $t_4$ and $t_6$ the stress exceeds the tensile strength which causes spallation; the dashed lines would describe further wave propagation if the crack had no influence.

where $\rho_s$ is the density of the specimen. The determination of the UHPC's wave speed bases on the time shift of the signals measured at a specified distance. This requires a longer specimen for sufficient accuracy. We obtained in this way an averaged elastic modulus of $E_{\text{dyn}} = 52\,\text{GPa}$ which is very similar to the value calculated from equation (4).

## 4 Determination of the dynamic tensile strength

For spallation experiments the experimental setup of Figure 1 is modified in such a way, that the specimen is placed at the end of the incident bar. The specimen is longer and has a free rear face. When the striker, launched by the air gun, hits the incident bar it generates a compressive pulse. This pulse propagates through the incident bar and, after some reflection at the interface, into the specimen. Here it is reflected at the free end. Phase inversion turns the compressive pulse into a tensile one and a superposition of incoming and reflected wave leads to a state of tension. The specimen will fracture if this tensile stress exceeds the material's strength. The situation in the specimen is illustrated in Figure 3 for a compressive pulse with a tension tail. The incoming wave is reflected at the rear face which induces a superposed wave front and a tensional stress state. Clearly, amplitude and position of the peak stress are defined by the shape of the wave and if, for example, the incoming wave is purely compressive, the maximum tension would simply follow from an inversion. This implies, that for a well defined wave superposition the specimen should be longer then the stress pulse. In our experiments the amplitude of the compressive stress pulse is about 20 MPa, with little tension tail, and has a length of 40–45 $\mu$s.

The dynamic tensile resistance $R_m^t$ is the maximum tension the material can sustain. When the superposed wave exceeds this value the specimen will fail and two fragments result. Brittle materials like UHPC have a low fracture energy and break by cleavage, i.e., the fractured surfaces are flat, unstructured and almost perpendicular to the axis of the specimen. Therefore, only a portion of the stress wave's energy is dissipated and the process of wave propagation and superposition will continue within the fragments. Depending on the energy of the incoming wave, additional cracks may occur.

Several fractured UHPC specimens are shown in Figure 4. We see at the first glance that the spallation experiment gives reproducible results, i.e., the cracks are at the same position in every specimen. It should be noted, that the 'crack of interest' for us is the backside crack which occurs at a distance of about 44 mm from the rear end. After fragmentation both fragments move with different velocities and about 40 $\mu$s later, after another reflection, the second crack appears. We use here the first

**Fig. 4.** UHPC specimens fractured in the spalling tests (left) and a typical fracture surface (right).

spallation because its position is crack is easier to focus with the fast cam, but selected measurements with the second crack confirmed the obtained values.

Different approaches have been proposed to determine the tensile resistance from these experiments. Erzar and Forquin reviewed in [5] the pros and cons of three common methods which all rely on d'Alembert's solution of the uniaxial wave equation. The simplest way is to measure the incident and reflected waves, 'shift' them to the later identified crack position $x_c$ and to determine the superposed elastic stress state there. The dynamic tensile strength is then defined as the level of the tensile stress reached at the location of fracture, $R_m^t = \sigma(x_c)$. This approach corresponds to the method illustrated in the drawing of Figure 3 and has been used, e.g. in [5,8,28]. It requires measurements with strain gauges for every specimen and relies on the fact, that the material behaves linear elastically and there is neither damage nor dissipation in the specimen before cracking. With these assumptions the dynamic tensile strength of the studied UHPC specimens is determined to $19.8 \pm 0.5$ MPa.

Another common method to derive the dynamic tensile strength exploits the fact, that the wave's particle velocity is reflected at the specimen's end and the superposition of incoming and reflected wave results in a velocity jump at the rear face. This so-called pullback velocity $\Delta v(l_s) = v_{\mathrm{pb}}$ can be measured by means of an accelerometer and is then translated into the corresponding stress amplitude, $\sigma = {}^1\!/_2 \rho c_L v_{\mathrm{pb}}$. The method seems to work for large and heavy specimens which have a high inertia [12,29–31]. The accuracy of measurement has limits when the specimen itself is accelerated by the impact. In our small samples it rather difficult to distinguish 'rigid' and particle velocity and to clearly identify the difference in velocity at the rebound of the rear face.

Our way of evaluating the tensile strength is to directly observe the spallation experiment and to define the stress at the instance of cracking as the tensile resistance. This decohesion stress $\sigma_c$ is approximated by the velocity difference of the fragments in the moment of spalling.

$$R_m^t \equiv \sigma_c = \rho\, c_L \Delta v = \rho\, c_L |v_{s,1} - v_{s,2}|. \tag{6}$$

Here $v_{s,1}, v_{s,2}$ denote the axial velocities of the crack flanks. The accuracy of relation (6) strongly depends on the quality of the velocity measurement, cf. [8], wherefore we employ a precise successive picture capturing by high-speed photography and digital image correlation. Again, the underlying theoretical considerations assume a superposition of elastic waves which leads to ideal cleavage of the specimen but they do not exclude previous damage or microscopic damping in the specimen.

Here a full set of 23 specimens has been tested. Eight experiments failed because of flawed specimen (air bubbles) which lead to damage at the front end or to slanted cracks. The averaged tensile resistance values obtained at a strain rate of 30 $s^{-1}$ is

$$R_m^t = 17.8 \pm 1.6 \text{ MPa}.$$

The tensile strength of UHPC is in the expected range of about one-tenth of its compressive resistance. The mechanical properties of the low silica UHPC mixture seems be very similar to established recipes where values of $R_m^t = 8 \ldots 40$ MPa are reported in [32–35].

## 5 Numerical simulations

In order validate our experimental observations we simulate the HPB experiment numerically. Because there is no commercial finite element software for dynamic crack propagation with a priori unknown crack path we used a specifically developed axisymmetric code here. To locate the crack an adaptive cohesive element technique is employed. This technique bases on the crack tip opening displacement model of Dugdale [36] and Barenblatt [37] where fracture is assumed to happen along a crack zone controlled by the traction on the crack flanks. Within a FEA framework cohesive interface elements are inserted between the continuum finite elements to model crack opening. Here we combine the cohesive element approach with an automatic element insertion procedure. This approach has proven to be reliable and efficient for numerous applications, see among others [38–41].

The cohesive elements follow a traction separation law which models locally the loss of cohesion during cracking. Simplifying the three-dimensional relations we state here the traction, i.e. the normal stress $\sigma$, to be a function of the effective opening displacement $\delta$. The crack opening starts at a critical cohesive traction $\sigma_c$ and ends when a critical opening displacement $\delta_c$ is attained. Here no traction can be transmitted anymore—the cohesive element is open. This situation maps a crack and the adjacent continuum elements are de-facto disconnected.

A typical traction-separation relation is the universal binding law of Smith and Ferrante [42,43], with the loading envelope

$$\sigma(\delta) = \mathrm{e}\,\sigma_c \frac{\delta}{\delta_0} \cdot \exp\left(-\frac{\delta}{\delta_0}\right), \tag{7}$$

where $\delta_0$ is the position of the maximal traction and e is the Euler number. Crack growth is then characterized by the loading conditions $\delta(t) = \max(\delta)$ and $\dot{\delta} \geq 0$; all other states correspond to unloading which is commonly assumed to be linear to the origin. In dynamic fracture the cohesive law 7 can be simplified by the linear loading envelope

$$\sigma(\delta) = \sigma_c \left(1 - \frac{\delta}{\delta_c}\right). \tag{8}$$

Figure 5 shows both cohesive laws. The area under the curves is the specific fracture energy, e.g.,

$$\mathcal{G}_c = \frac{1}{2}\sigma_c \delta_c. \tag{9}$$

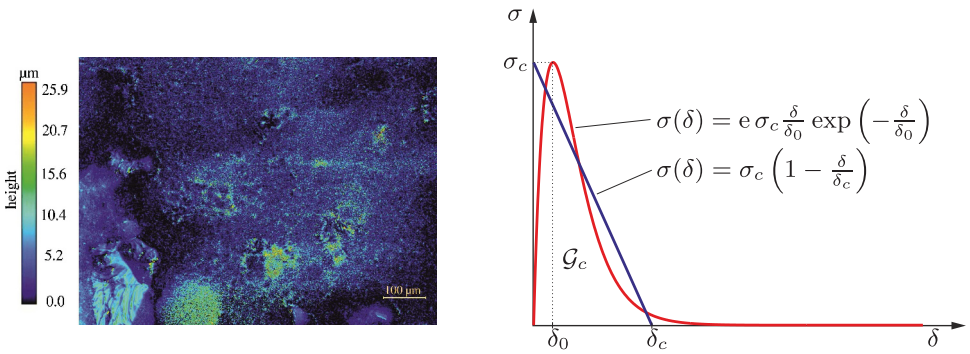


**Fig. 5.** Typical surface profile of a spalled UHPC specimens and cohesive traction-separation law for cracking: exponential law (red) and linear cohesive envelope (blue).

Our specimen is meshed uniformly with triangular finite elements. From the strain pulse measured in the incident bar, the difference in impedance, and a low amplitude pulses measured in the specimen we conclude on the shape of the stress pulse entering the specimen. It is applied as load on the (front) boundary. The analysis proceeds incrementally in time. In order to reproduce the propagating wave correctly we use for time discretization a central difference scheme with weighted displacement field. More numerical details can be found in [44].

A cohesive element will be added to the mesh if the local tension exceeds the cohesive strength $\sigma_c$ which is for brittle material identified with the tensile resistance $R_m^t$. Thus, in every time step of the calculations, this condition is checked for each internal face and the faces where the criterion is met are flagged for subsequent processing. Cohesive elements are inserted at all flagged faces and, subsequently, the elements open in tension whereas in compression contact conditions apply. Once the opening has exceeded $\delta_c$, a crack has formed. In this manner, the shape and location of a successive crack front is itself an outcome of the calculations.

Aside of the cohesive strength $\sigma_c$ a second parameter is required to determine the cohesive law, namely either the critical opening displacement $\delta_c$ or the specific fracture energy $\mathcal{G}_c$. Here we decide to determine $\delta_c$ via a fractography of the broken specimens. A KEYENCE VK9700K microscope using a laser confocal technology with a short wave laser light source and a white light source, was utilized to provide focused images for the entire depth of the surface, see Figure 5. For the specific impact velocity of our experiments the surface heights, measured from the deepest point after fracture, vary up to 26 $\mu$m. This motivated us to assume an 'averaged' crack opening displacement of 10 $\mu$m. This value for $\delta_c$ is small and corresponds to a specific fracture energy of $\mathcal{G}_c = 75\,\mathrm{N/m}$ which, in turn, is a realistic value for ceramic like materials.

At first we vary the cohesive stress $\sigma_c$ in order to determine its effect on crack growth. We start with the experimental value of 17 MPa and see that cohesive elements are inserted at the expected position of crack growth, namely at about 45 mm from the rear end of the specimen. A small, localized crack zone develops. Slight deviations of $\sigma_c$ are possible and we get basically the same result for $\sigma_c = 16 \ldots 18\,\mathrm{MPa}$. A higher value of $\sigma_c = 20\,\mathrm{MPa}$, however, does not lead to any insertion of cohesive elements and so no crack can form. The cohesive stress is obviously to high. If we choose lower values of $\sigma_c \leq 15\,\mathrm{MPa}$, the cohesive elements will be inserted earlier, i.e., the crack moves towards the free end, see Figure 6. This follows from the fact that the reflected pulse $\sigma$ reaches the value of $\sigma_c$ earlier, cf. Figure 3. Moreover, lowering $\sigma_c$ gives a wider zone of many cohesive elements which will be partially opened.

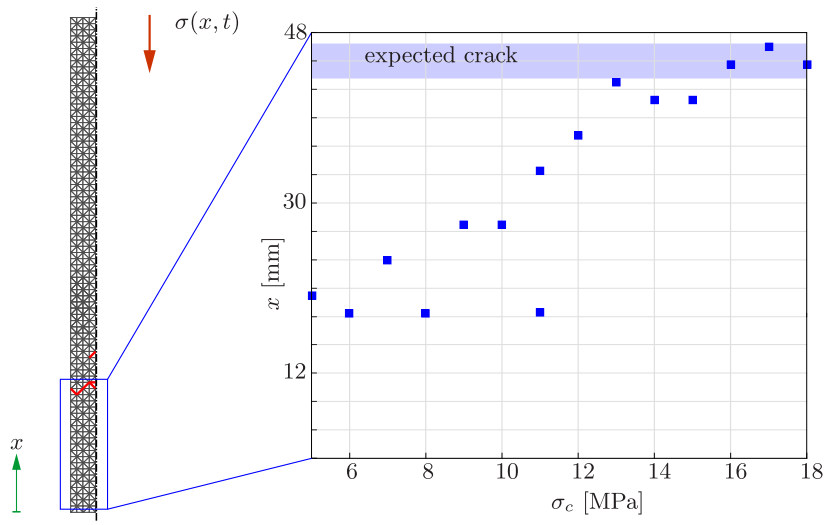


**Fig. 6.** One symmetry half of the specimen at the end of the finite element simulation and influence of the decohesion stress $\sigma_c$ on the position of the adaptively inserted cohesive elements. The actual calculations are performed with 2560 elements, i.e., each triangle of the mesh in Figure 6 is refined into four elements.

This would correspond to a distributed damage and does not match our experimental observations.

At next we determine the fragments velocities in our finite element simulation. For $\sigma_c = 17\,\text{MPa}$, $\delta_c = 10\,\mu\text{m}$ and $\Delta v = |v_{s,1} - v_{s,2}|$ we obtain $\Delta v = 2.72$ m/s and equation (6) gives a tensile resistance of 29.8 MPa. This value is still meaningful but obviously to high. Major reason for the large velocity difference is the numerical dissipation of the cohesive element technique which mainly results from the insertion (and partial opening) of some unnecessary elements. Please note that variations of $\delta_c = 5 \ldots 15\,\mu\text{m}$ had little influence. Also, further studies with the exponential cohesive law 7 show a very similar behavior in variations of $\sigma_c$ and $\delta_0$. Other studies with a completely different numerical method (a phase-field fracture approach) give results were the $\Delta v$ is rather under-than overestimated [45].

Concluding we state, that the measured value for the tensile resistance of low-silica UHPC is confirmed by the cohesive stress in our numerical simulations.

## 6 Conclusion

A breakthrough is achieved by production of ultra-high performance concrete (UHPC) as new generation of concrete. Very high compressive strength and very dense microstructure is obtained by the new concrete mix design. In this paper, some mechanical properties of this material are experimentally determined. In this respect, UHPC specimens are fabricated and series of dynamic tests are conduct by split Hopkinson pressure bar (SHPB). By the experiments the dynamic modulus of the UHPC specimens is determined. Furthermore, based on series of the spalling tests at strain rate of 30 $s^{-1}$, dynamic tensile strength of studied specimens is determined. Since the dynamic parameters, which are measured in the experiments, are strongly influenced by the experimental setup, calibration of SHPB was performed precisely, and dynamic stress equilibrium condition was provided. Modification on the incident

pulse by a proper pulse shaper is obtained and it is facilitated a constant strain-rate loading. The values of $19.5 \pm 0.9$ MPa and $17.8 \pm 1.6$ MPa are obtained for the dynamic tensile strength of the studied UHPC specimens based on pull back velocity and decohesion stress, respectively. The obtained results can not only be used in order to develop new types of UHPC material, but can also be used for future computational models.

## References


1. E. Fehling, M. Schmidt, J. Walraven, T. Leutbecher, S. Fröhlich, in *Ultra-high performance concrete UHPC: fundamentals, design, examples* (Wiley, 2014), p. 198
2. C. Albertini, E. Cadoni, K. Labibes, Exp. Mech. **39**, 137 (1999)
3. C. Bludau, Jahrgang Beton- und Stahlbetonbau **39**, 17 (2005)
4. A. Brara, J.R. Klepaczko, Mech. Mater. **38**, 253 (2006)
5. B. Erzar, P. Forquin, Exp. Mech. **50**, 941 (2010)
6. B. Erzar, P. Forquin, Int. J. Solids Struct. **41**, 2259 (2014)
7. C. Pontiroli, B. Erzar, E. Buzaud, Key Eng. Mater. **711**, 171 (2016)
8. J.R. Klepaczko, A. Brara, Int. J. Impact Eng. **25**, 387 (2001)
9. H. Wu, Q. Zhang, F. Huang, Q. Jin, Int. J. Impact Eng. **32**, 605 (2005)
10. M. Daimaruya, H. Kobayashi, H. Shizawa, R.A. Sirega, Y. Ishihata, in *Proceedings of 10th international conference on fractures, Hawai*, edited by W. Gerberich (2001), p. 9
11. L. Daudeville, Y. Malecot, Eur. J. Environ. Civ. Eng. **15**, 101 (2011)
12. H. Schuler, C. Mayrhofer, K. Thoma, Int. J. Impact Eng. **32**, 1635 (2006)
13. J. Weerheijm, I. Vegt, in *Proceedings of fracture mechanics of concrete and concrete structures, Seoul*, edited by B.H. Oh, et al. (2010), p. 419
14. J. Weerheijma, J.C.A.M. Van Doormaal, Int. J. Impact Eng. **34**, 609 (2007)
15. L. Zhang, S.S. Hu, D.-X. Chen, Z.-Q. Yu, F. Liu, Exp. Mech. **49**, 523 (2009)
16. A. Caverzana, M. Peroni, G. Solomos, Eur. Phys. J. Special Topics **225**, 283 (2016)
17. F.G. Diaz-Rubio, J.R. Perez, V.S. Galvez, Int. J. Impact Eng. **27**, 161 (2002)
18. M.J. Perez-Martin, B. Erice, D.A. Cendon, F. Galvez, Eur. Phys. J. Special Topics **206**, 117 (2012)
19. DIN 1045-2, Deutsches Institut für Normung (2008)
20. K. Weinberg, M.R. Khosravani, B. Thimm, T. Reppel, L. Bogunia, S. Aghayan, R. Nötzel. GAMM-Mitteilungen (2018) (in press)
21. H. Kolsky, in *Stress waves in solids* (Dover Books on Physics, New York, 1963), p. 214
22. W. Chen, B. Song, in *Split Hopkinson (Kolsky) Bar.* (Springer, New York, 2011), p. 388
23. Q.M. Li, H. Meng, Int. J. Solids Struct. **40**, 343 (2003)
24. X.Q. Zhou, H. Hao, Int. J. Solids Struct. **45**, 4648 (2008)
25. Y. Lu, K. Xu, Int. J. Solids Struct. **41**, 131 (2004)
26. J. Yang, G-F. Peng, Y-X. Gao, H. Zhang, Key Eng. Mater. **629**, 96 (2015)
27. S. Kim, J. Park, D. Yoo, Y. Yoon, in *Proceedings of HiPerMat 2012. 3rd international symposium on UHPC, Kassel*, edited by M. Schmidt, et al. (2012), p. 317
28. F.G. Diaz-Rubio, J. Rodriguez Perez, V. Sanchez Galvez, Int. J. Impact Eng. **27**, 161 (2002)
29. S.A. Novikov, I.I. Divnov, A.G. Ivanov, Phys. Met. Metall. **21**, 608 (1966)
30. S.A. Novikov, A.V. Chernov, J. Appl. Mech. Tech. Phys. **23**, 703 (1982)
31. M. Nöldgen, O. Millon, K. Thomas, E. Fehling, Beton- und Stahlbetonbau **104**, 717 (2009)
32. M. Nöldgen, Ph.D. thesis, Kassel University, 2010
33. O. Millon, W. Riedel, C. Mayrhofer, K. Thoma, in *Proceedings of HiPerMat 2012. 3rd international symposium on UHPC, Kassel*, edited by M. Schmidt, et al. (2012), p. 101
34. M. Orgass, Y. Klug, in *Proceedings of the international symposium on UHPC, Kassel*, edited by M. Schmidt, et al. (2004), p. 637

35. J.C. Scheydt, O. Millon, H.S. Muller, K. Thoma, Beton-und Stahlbetonbau **107**, 289 (2012)
36. D.S. Dugdale, J. Mech. Phys. Solids **8**, 100 (1960)
37. G.I. Barenblatt, Adv. Appl. Mech. **7**, 55 (1962)
38. C. Yu, A. Pandolfi, M. Ortiz, D. Coker, A.J. Rosakis, Int. J. Solids Struct. **39**, 6135 (2002)
39. I. Scheider, W. Brocks, Comput. Mater. Sci. **37**, 101 (2006)
40. A. Ferrara, A. Pandolfi, Comput. Methods Biomech. Biomed. Eng. **11**, 553 (2008)
41. A. Pandolfi, K. Weinberg, Eng. Fract. Mech. **78**, 2052 (2011)
42. J. Ferrante, J.R. Smith, J.H. Rose, Mater. Sci. Eng. **7**, 19 (1981)
43. A. Needleman, Int. J. Fract. **42**, 21 (1990)
44. K. Weinberg, T. Dally, C. Bilgen, Theor. Appl. Fract. Mech. (2017) (submitted)
45. T. Dally, K. Weinberg, Continuum Mech. Thermodyn. **29**, 947 (2017)